Supplementary Material: Transient subglacial water routing efficiency modulates ice velocities prior to surge termination on Sít' Kusá, AK.

Yoram TERLETH, Timothy C. BARTHOLOMAUS, Jukes LIU, Flavien BEAUD, T. Dylan MIKESELL, Ellyn M. ENDERLIN

S1 Seismic tremor time-series

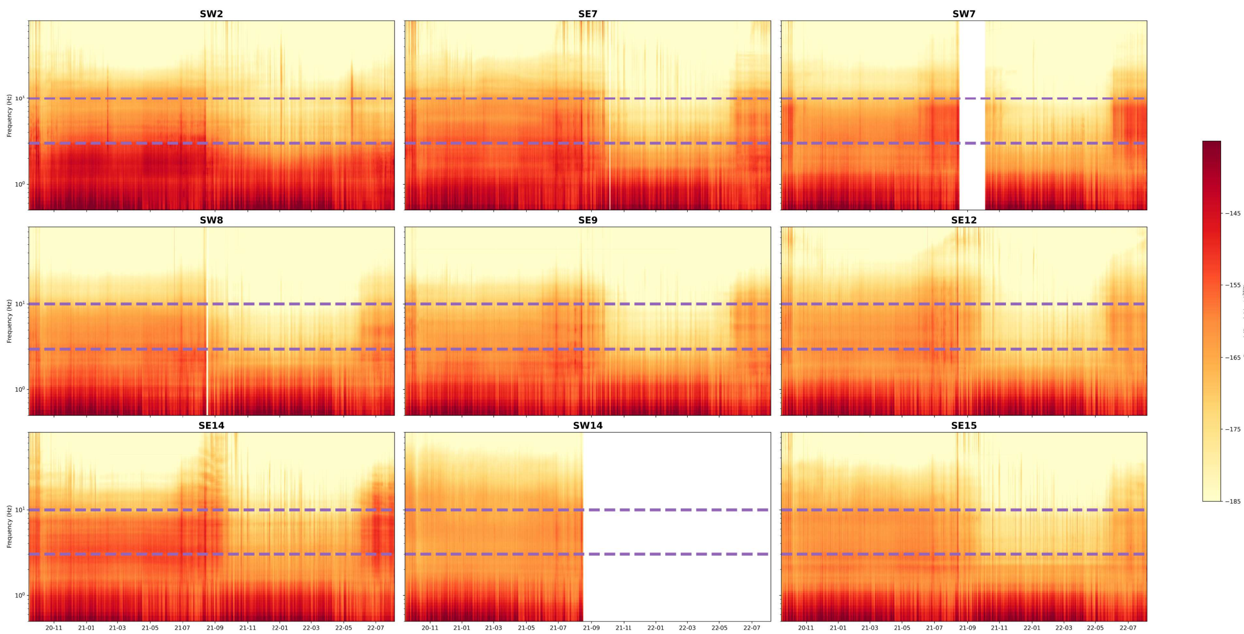

Figure S1.1: Spectrograms of the median power of 60 min, 50% overlapping time windows of vertical channel seismic data from functioning stations of the network shown in Fig.1 of the main text. The 3-10 Hz frequency range is bounded by dotted lines.

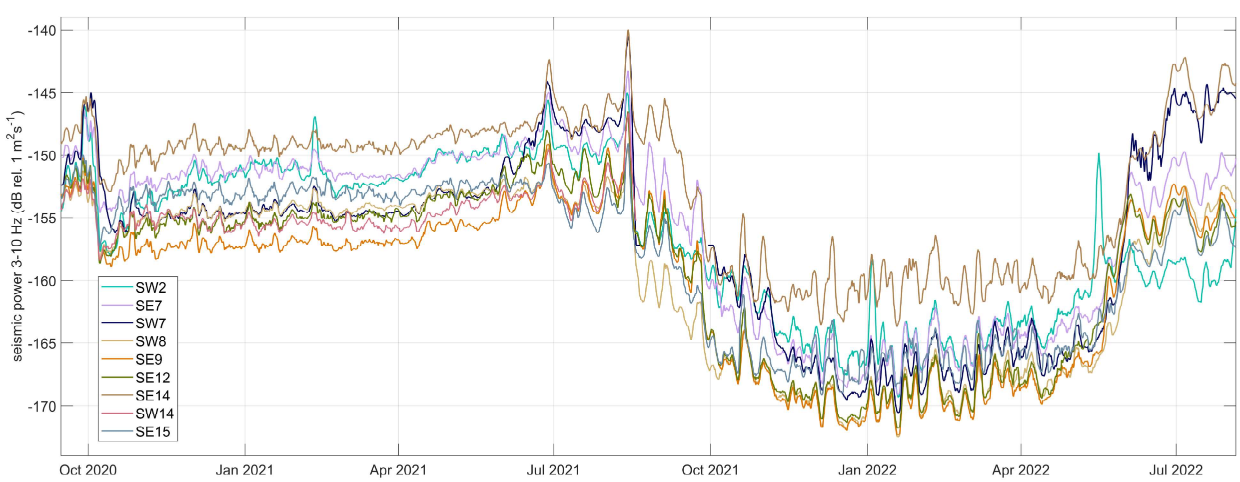

Figure S1.2: Time-series of seismic tremor power integrated between 3-10 Hz, with a 72 hour moving average filter applied.

S2 Noise sourced by calving events below 3 Hz.

Text S2

Fig.S2.1 shows the spectrogram for SW2 along with the the tremor signal power when integrated between 1.5-10 Hz (Bartholomaus et al. 2015) and 3-10 Hz (this paper). The broader frequency window yields higher power and correlates more closely with the number of STA/LTA detections for a signal band-passed to the 1-3 Hz frequency range. The difference in amplitude between the two frequency windows in Fig.S2.1 **(b)** increases in November 2020, when the Sít' Kusá terminus reaches the ocean.

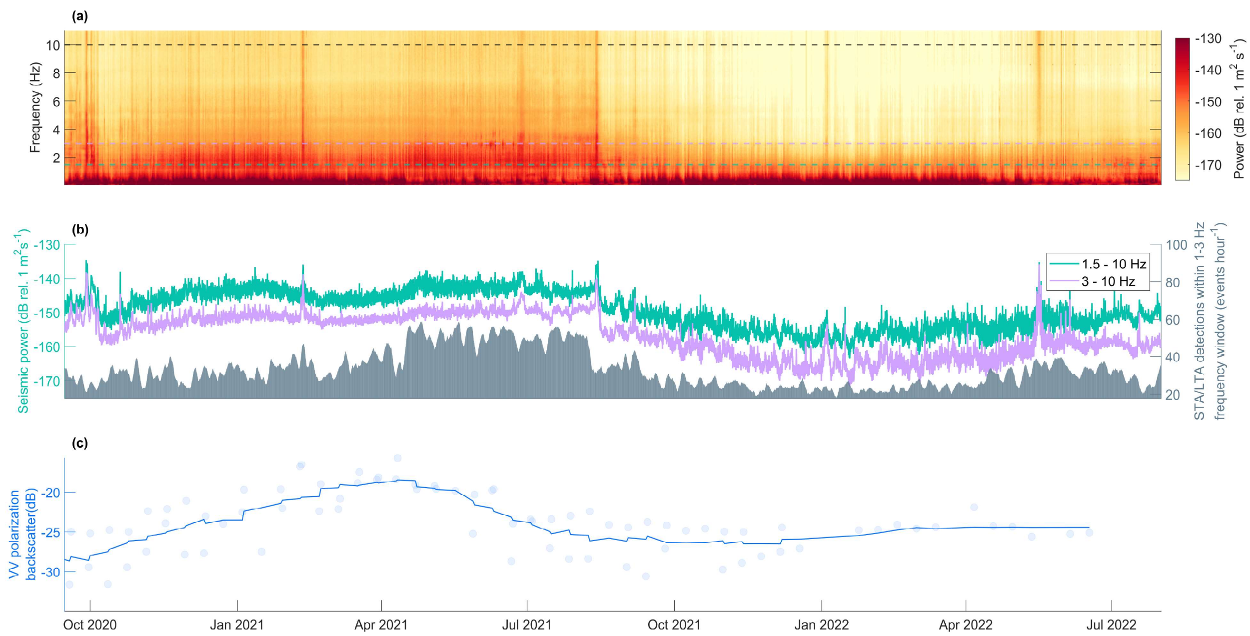

Figure S2.1: **a)** Spectrogram of 30 min median power for SW2. 10 Hz highlighted in grey, 3 Hz highlighted in purple, 1.5 Hz highlighted in blue. **b)** Tremor recorded in 1.5-10 Hz and 3-10 Hz frequency bands. Grey bars show number of STA/LTA detections per hour at SW2, with window lengths of 3.5 seconds and 60 seconds aimed towards detecting calving events. **c)** Total backscatter in VV polarization from Sentinel-1 SAR imagery within the AOI defined in main text.

S3 Energy Balance Firn Model

a) Model Forcing Data Overview

Table S3.1: Overview of input data used in EBFM surface energy balance model. ECWMF stands for European center for medium range forecasts. CRREL stands for cold regions research and engineering laboratory. Geographical locations of Haenke Island AWS and ERA-5 grid-call shown in Figure 1 of the main text.

Data	Location	Type	Temporal Resolution	Period	Source
Air Temperature	Haenke Island	AWS observation	0.25 h	Jul. 2020 - Oct. 2021	CRREL
Air Temperature	grid-cell (5.5 km×16.5 km)	ERA-5 reanalysis	1 h	Nov. 2021 - Aug. 2022	ECWMF
Surface Pressure	Haenke Island	AWS observation	0.25 h	Jul. 2020 - Oct. 2021	CRREL
Surface Pressure	grid-cell (5.5 km×16.5 km)	ERA-5 reanalysis	1 h	Nov. 2021 - Aug. 2022	ECWMF
Relative Humidity	Haenke Island	AWS observation	0.25 h	Jul. 2020 - Oct. 2021	CRREL
Relative Humidity	grid-cell (5.5 km×16.5 km)	ERA-5 reanalysis	1 h	Nov. 2021 - Aug. 2022	ECWMF
Precipitation	grid-cell (5.5 km×16.5 km)	ERA-5 reanalysis	1 h	Jul. 2020 - Aug. 2022	ECWMF
Cloud cover	grid-cell (5.5 km×16.5 km)	ERA-5 reanalysis	1 h	Jul. 2020 - Aug. 2022	ECWMF

b) Assessment of EBFM performance

Text S3b

There is a paucity of surface mass balance observations on SK. In order to provide an assessment of the performance of the EBFM and our surface runoff estimations, we compare the modelled surface elevation change at a series of sample points with surface elevation change observed by differentiating digital elevation models (DEMs). The DEMs are derived from Worldview satellite imagery © 2022 Maxar, following the Ames stereo pipeline described in Shean et al. (2016). We select a series of sites that are spatially spread out along the available DEMs, and that are not heavily crevassed. We assume that all surface elevation change is driven by climatic mass balance (emergence/submergence velocities are neglected). We find R^2=0.88 and RMSE=1.31 between the observed and modelled values.

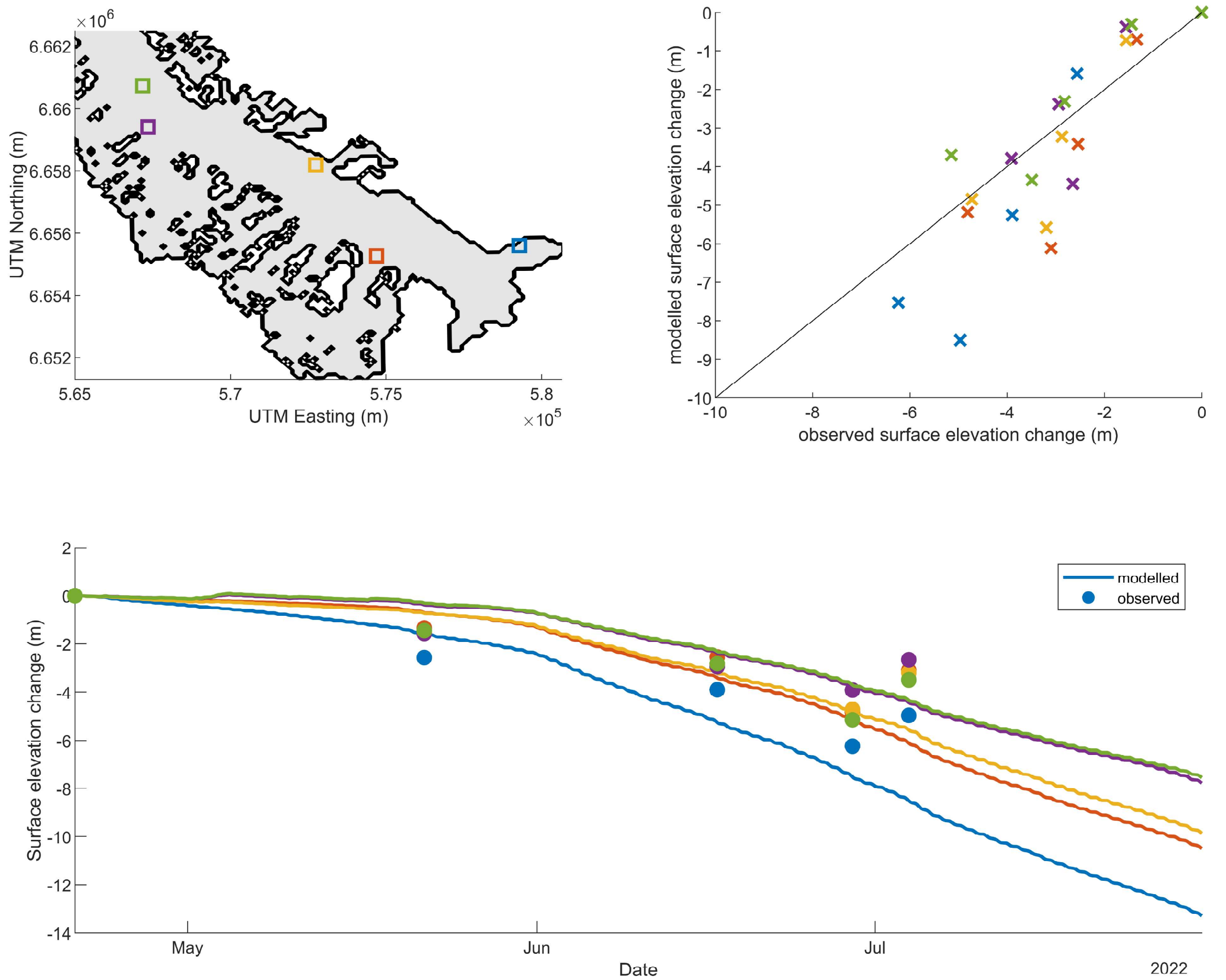

Figure S3.1: Sampling locations, model performance scatter-plot and timeseries of observed and modelled elevation change over the spring of 2022.

c) Spatial integration of surface runoff

Text S3c

During installation of the field instruments, the surface of the glacier was already extremely crevassed throughout the southern tributary and the main trunk. Figure 6 in the main text provides an example of the nature of the glacier surface. Supra-glacial water routing would be extremely limited along such a surface. The extensive crevassing would also favor rapid englacial transfer of water to the bed (e.g. Sevestre et al. 2018) and we assume that water from surface runoff quickly penetrated to the bed.

The surface runoff variable in the EBFM output provides a spatially distributed estimate of the water leaving the bottom of the snow/firn pack, or surface melt directly when the surface is bare ice. However, for the purposes of this work we are interested in the (subglacial) discharge, and we would rather have an estimate of possible water supply to any region of the glacier bed. As such, we integrate the total surface runoff above any point of the glacier.

We use the surface topography as an input to the `drainagebasins` and `flowacc` functions of the Matlab topotoolbox (Schwanghart & Scherler 2014) to simulate flow accumulation over the glacier from the spatially distributed surface runoff. The function yields discrete water pathways, which we smooth out spatially using a 1.7 km^2 kernel (Fig.S3.2).

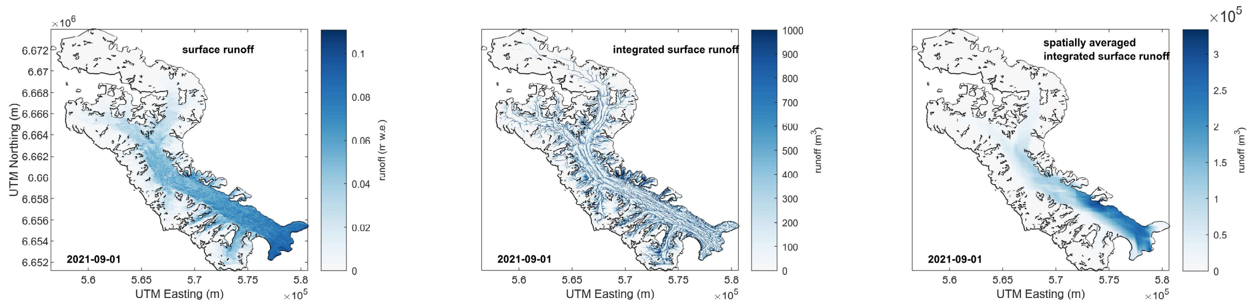

Figure S3.2: Integration and spatial averaging of surface runoff along modelled subglacial flow accumulation.

S4 Seismic Noise - Sliding correlation

Text S4

We suggest our timeseries of seismic tremor in the 3-10 Hz band are predominantly hydraulic in origin. Here we present further justification for this suggestion and assess possible contributions from seismic tremor source by basal sliding to those timeseries.

We first focus on the period between 1 October and 15 November 2020 (Fig.S4.1), because we have GPS based surface speed measurements available, ice velocities are high, and there is a transition out of the melt-season. There is high correlation between surface runoff and tremor, and no significant correlation between sliding velocity and tremor. We observe persistent coherence between tremor signals at different locations of the glacier in addition to lag times of several hours between the coherent timeseries. These data increase our confidence that the observed tremor signals are predominantly hydrologic in origin rather than caused by slow gliding tremor (Lipovsky et al. 2019) or high numbers of low frequency stick slip events (e.g. Umlauft et al. 2021; Köpfli et al. 2022), even during the 2020-2021 winter.

Over our entire record of observations, the correlation between modelled surface runoff and the SE7 tremor signal is ∼0.52 and remains significant at the 95% confidence level.

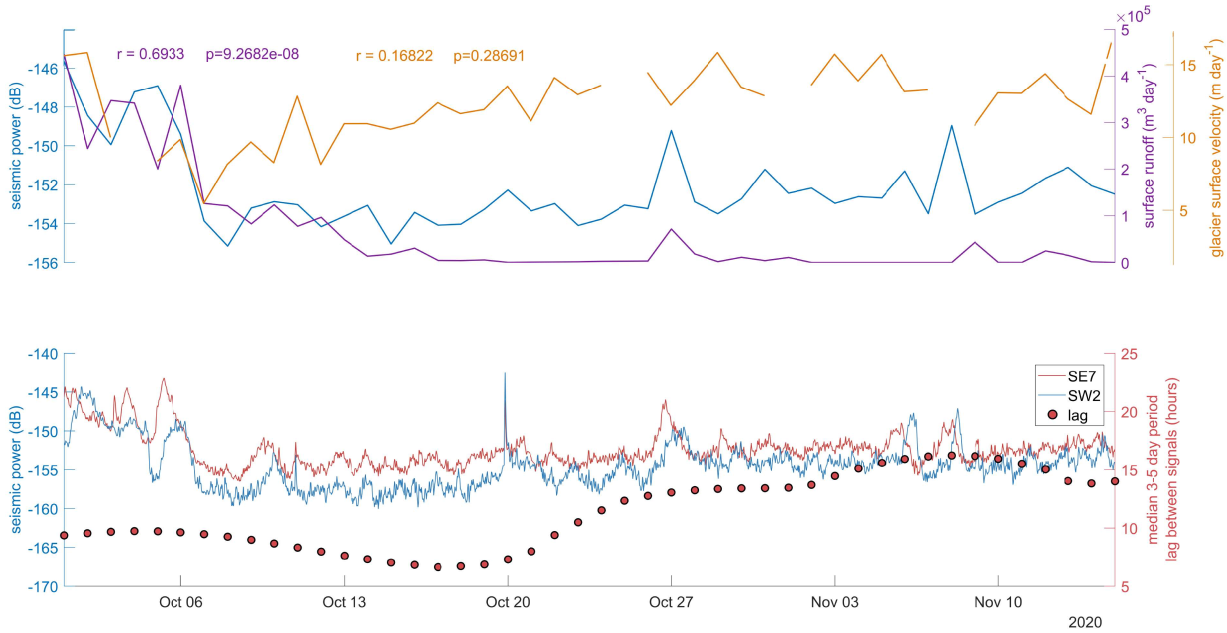

Figure S4.1: Upper panel shows time series of seismic tremor power in the 3-10 Hz range measured at SW14, glacier surface velocity measured at G14, and modelled surface runoff. Correlation and p-value between seismic tremor and both runoff and ice velocity for the plotted period shown on plot. Lower panel shows seismic power at SE7 and at SW2, with the lag between the tremor signals recorded at the two stations for the same time period.

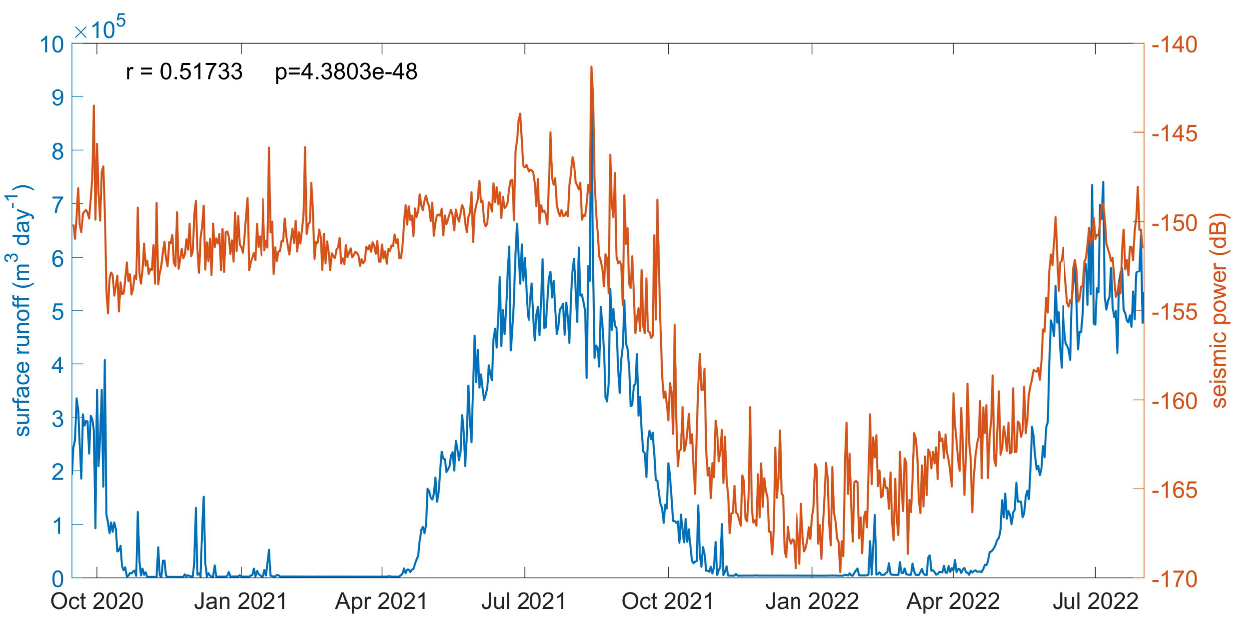

Figure S4.2: Plot showing tremor power between 3 and 10 Hz at SE7 and modelled surface runoff for the entire record of observation. Correlation coefficient and significance level are shown on plot.

S5 Time-lags

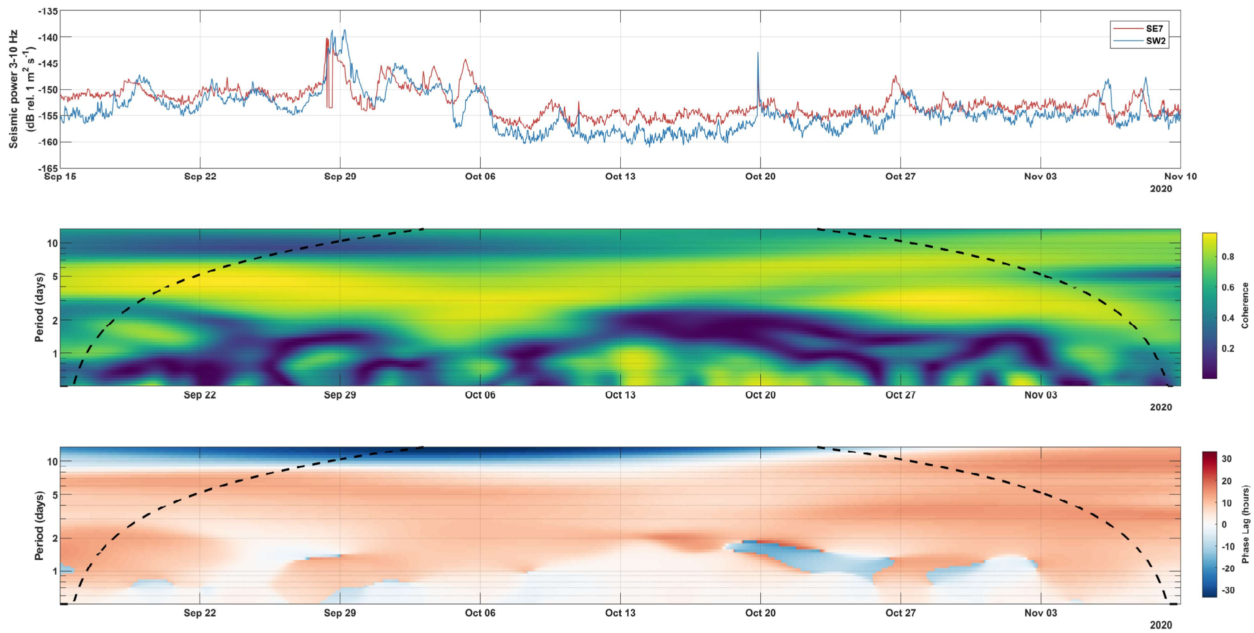

Figure S5.1: Plot showing tremor power timeseries at SE7 and SW2, coherence in time/frequency space between the two timeseries, and time-lags between the two timeseries.

Text S5

Here we include further discussion regarding the drivers of the various lag times. In Figures 2 and 6 of the main text we show only the time-lags when the coherence between signals is above 0.7. In Fig.S5.1 we show the full time/frequency coherence and time/frequency time-lags plots. Fig.S5.2 is similar to Fig. 6 of the main text but shows the time-lags between SE7 and SW2. There is a brief period of coherence between 14 March and 24 March (green box), during which time-lags are negative, meaning tremor signal recorded at SW2 is ahead of the signal recorded at SE7. In our model estimate, there is no surface runoff produced anywhere on the glacier during this period. We interpret this behavior as the signature of an inefficient drainage system through which pressure pulses migrate upstream. The negative time-lags fall in the middle of a ∼2 month period with low coherence in the lower trunk. This further suggests that the lower trunk's drainage system went through a low efficiency and poorly connected phase during late winter of 2021.

In February 2022 (purple box), brief moments of surface runoff are reflected in the seismic tremor signals. During this time, SE7 is ahead of SW2, suggesting water or pressure pulse motion in the downstream direction. After February 16, we estimate that there is only very minor water supply from the surface, while we start observing negative time-lags. This could be due to upstream migration of pressure pulses as well, or it might be driven by distributed melt input dominating the tremor signal.

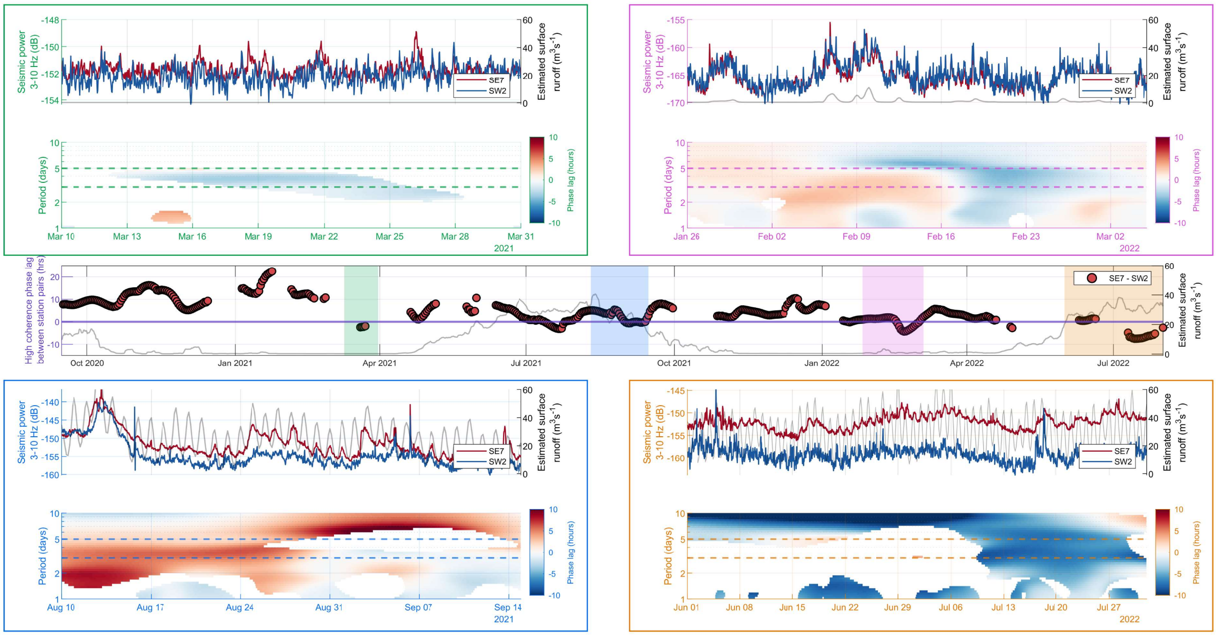

Figure S5.2: Phase lags between seismic tremor signals recorded at SE7 and SW2, with tremor signals and time/frequency lag plots shown for four highlighted periods. The estimated surface runoff at the bottom of the snow and firn layer is plotted on the lag and tremor plots for reference.

In August and September 2021 (blue box), we observe positive and low lag-times. Both tremor signals respond to the diurnal cycle in surface runoff, but the amplitude of the diurnal cycle is more muted at SW2. This hints at a connected drainage system through which water moves quickly from near SE7 to near SW2. In September 2021, there are negative time-lags with periodicity between 1 and 3 days, which seem driven by distributed melt influx.

In June and July 2022 (orange box), there is a diurnal cycle in both tremor signals, and low coherence through most of the time period. Starting on 13 July, there are strong negative time-lags. This seems driven by distributed melt influx, with variations occurring earlier at SW2 as there is less buffer from glacier snow cover.

Overviews of the lag times between the SE15-SE7 and SE7-SW2 station pairs are shown in Figures S5.3 and S5.4. In both cases, negative time-lags occur in late winter, through a combination of upward pressure pulse migration and differential distributed surface water supply, and late summer primarily through differential surface water supply. Negative time-lags, caused by similar differential surface runoff supply, occur commonly at a period of 1 day during both summers for both station pairs. This is likely the result of daily melt occurring earlier each day lower down on the glacier.

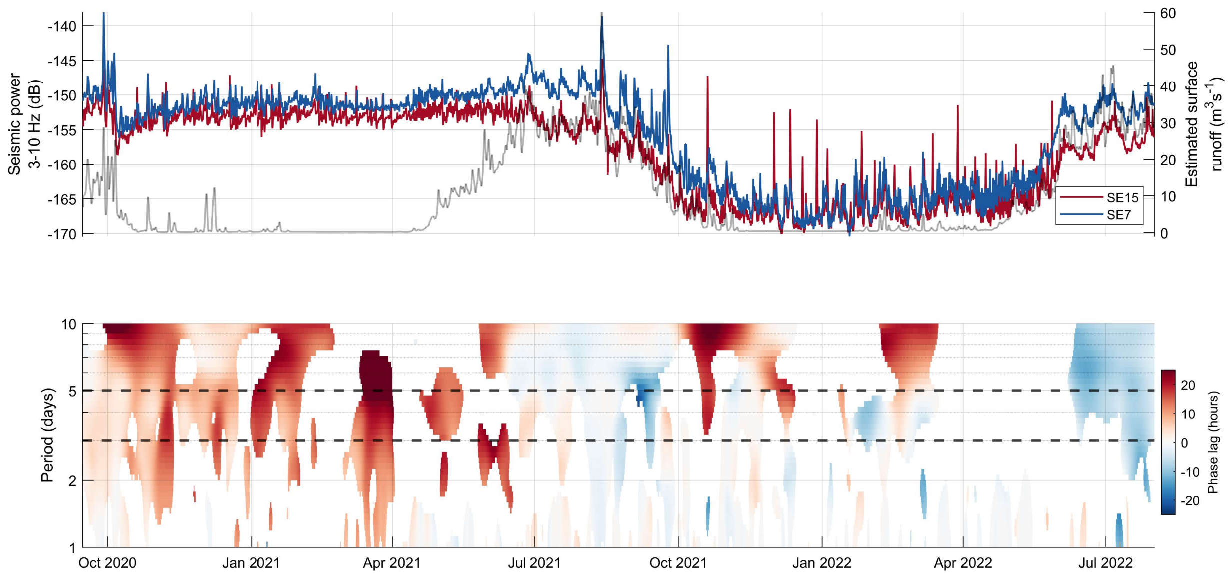

Figure S5.3: Overview showing SE15 and SE7 tremor time series, and lag-times between them in time/frequency space.

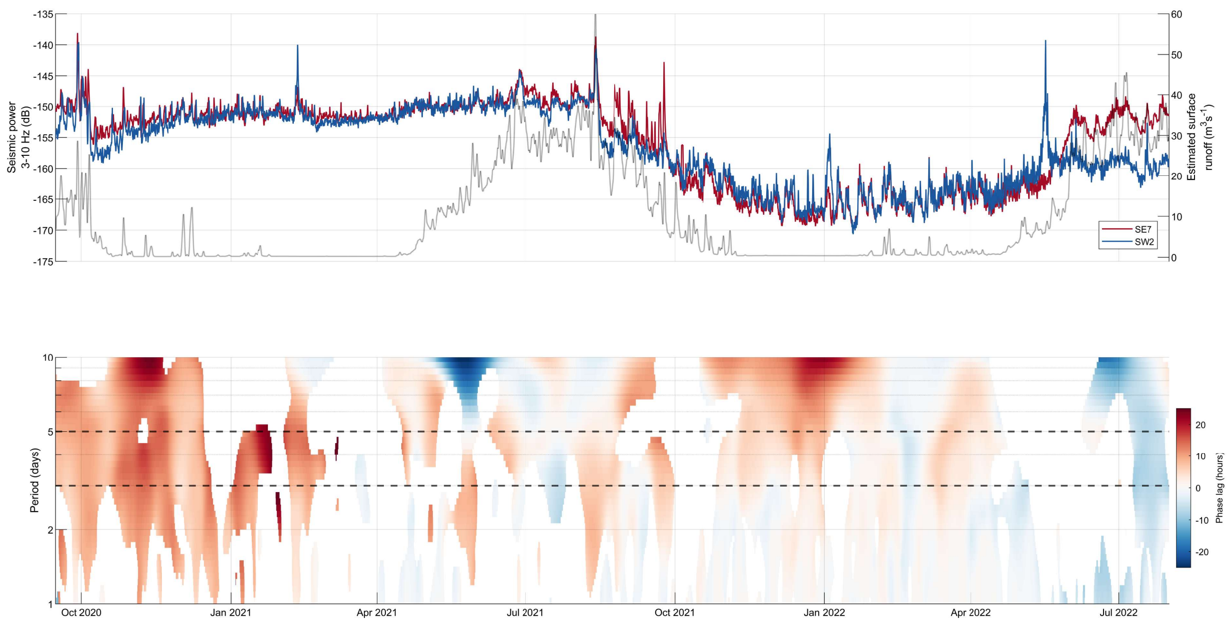

Figure S5.4: Overview showing SE7 and SW2 tremor time series, and lag-times between them in time/frequency space.

Fig.S5.5 shows the median time-lags for 3-5 day periods when signal coherence is above 0.7 between SE15 and all other stations. High time-lags (>5 hours) predominantly during the melt season, and briefly in February 2022. Lag times are less variable are more consistently positive, and less variable, during the surge (prior to summer 2021) than after the surge. We carefully suggest that this could be driven by consistent water supply to the subglacial drainage system from some sort of reservoir during the surge, while after termination this reservoir is exhausted and more poorly connected and lower volume drainage system adapts to the variable input of surface runoff.

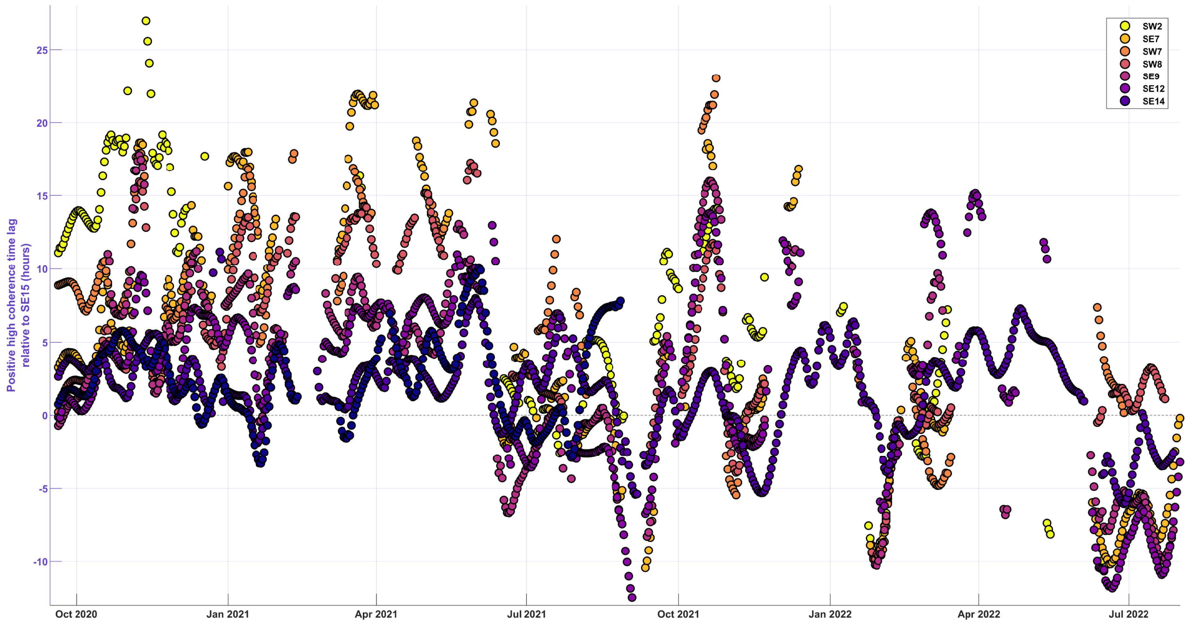

Figure S5.5: 3-5 day time-lags computed for all seismic stations relative to SE15.

S6 Subglacial Water Discharge at the Sít' Tlein Terminus

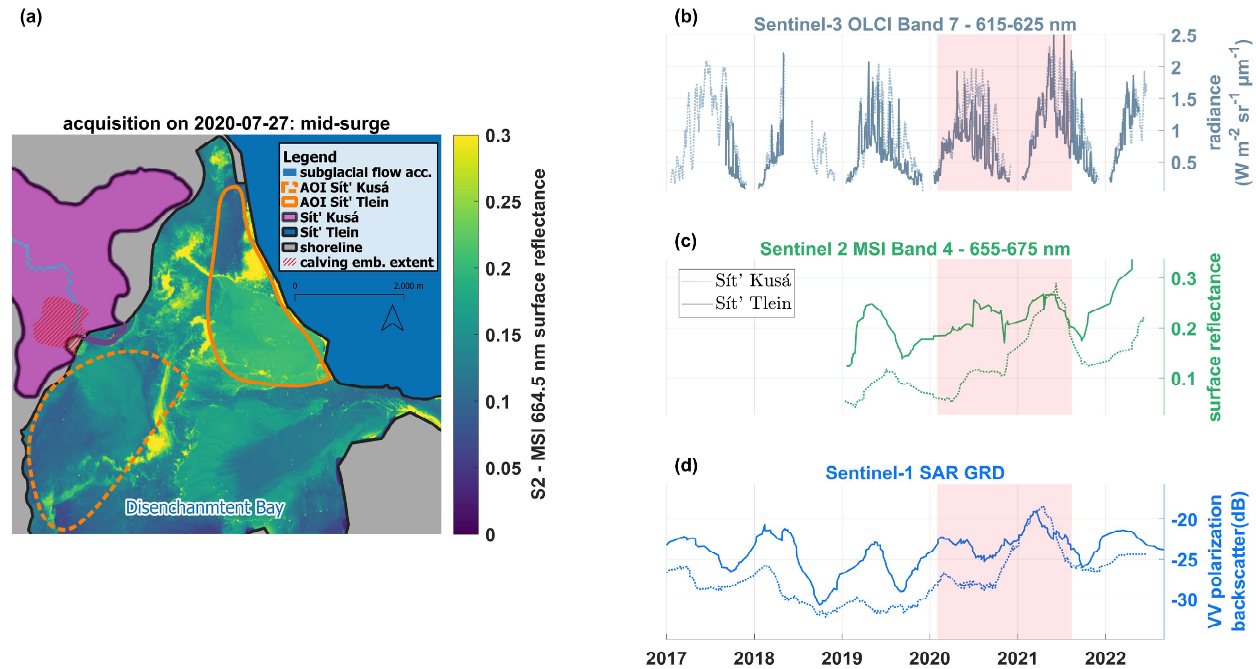

Figure S6.1: **(a)** False color showing surface reflectance in band 4 of Sentinel-2 MSI instrument. Image acquired on July 27th 2020, ∼5 months after surge initiation and 13 months before surge termination. Sít' Kusá RGI outline shown in purple, Sít' Tlein (Hubbard Glacier) outline shown in blue, and non glacierized shore shown in grey. Orange polygons shows areas of interest over which observations are averaged for each glacier. **(b)** Radiance in Sentinel-3 OLCI band 7. **(c)** Surface reflectance in Sentinel-2 band 4. **(d)** Sentinel-1 Synthetic Aperture Radar Ground Range Detected Vertical-Vertical-polarized back-scatter. Time-series show individual data points and a 10-point moving average. Full lines show values for the Sít' Tlein AOI while dotted lines show values for the Sít' Kusá terminus as a reference. Time-series show 10-point moving averages.

References

Bartholomaus T. C., Amundson J. M., Walter J. I., O'Neel S., West M. E., & Larsen C. F. (2015). Subglacial discharge at tidewater glaciers revealed by seismic tremor. *Geophysical Research Letters* 42.15, pp. 6391–6398. DOI: 10.1002/2015GL064590.

Köpfli M., Gräff D., Lipovsky B. P., Selvadurai P. A., Farinotti D., & Walter F. (2022). Hydraulic Conditions for Stick-Slip Tremor Beneath an Alpine Glacier. *Geophysical Research Letters* 49.21, e2022GL100286.

Lipovsky B. P., Meyer C. R., Zoet L. K., McCarthy C., Hansen D. D., Rempel A. W., & Gimbert F. (2019). Glacier sliding, seismicity and sediment entrainment. *Annals of Glaciology* 60.79, pp. 182–192. DOI: 10.1017/aog.2019.24.

Schwanghart W. & Scherler D. (Jan. 15, 2014). Short Communication: TopoToolbox 2 – MATLAB-based software for topographic analysis and modeling in Earth surface sciences. *Earth Surface Dynamics* 2.1, pp. 1–7. ISSN: 2196-6311. DOI: 10.5194/esurf-2-1-2014. (Visited on 02/14/2023).

Sevestre H., Benn D. I., Luckman A., Nuth C., Kohler J., Lindbäck K., & Pettersson R. (2018). Tidewater glacier surges initiated at the terminus. *Journal of Geophysical Research: Earth Surface* 123.5, pp. 1035–1051. DOI: 10.1029/2017JF004358.

Shean D. E., Alexandrov O., Moratto Z. M., Smith B. E., Joughin I. R., Porter C., & Morin P. (June 1, 2016). An automated, open-source pipeline for mass production of digital elevation models (DEMs) from very-high-resolution commercial stereo satellite imagery. *ISPRS Journal of Photogrammetry and Remote Sensing* 116, pp. 101–117. ISSN: 0924-2716. DOI: 10.1016/j.isprsjprs.2016.03.012. (Visited on 05/24/2023).

Umlauft J., Lindner F., Roux P., Mikesell T. D., Haney M. M., Korn M., & Walter F. T. (2021). Stick-slip tremor beneath an alpine glacier. *Geophysical Research Letters* 48.2, e2020GL090528.